A Multi-Frequency Radar Sounder for Lava Tubes Detection on the Moon : Design, Performance Assessment and Simulations

Leonardo Carrer, Christopher Gerekos, Lorenzo Bruzzone

Department of Information Engineering and Computer Science, University of Trento, Italy. Correspondence should be addressed to L.B. (email: lorenzo.bruzzone@unitn.it)

Abstract

Lunar lava tubes have attracted special interest as they would be suitable shelters for future human outposts on the Moon. Recent experimental results from optical images and gravitational anomalies have brought strong evidence of their existence, but such investigative means have very limited potential for global mapping of lava tubes. In this paper, we investigate the design requirement and feasibility of a radar sounder system specifically conceived for detecting subsurface Moon lava tubes from orbit. This is done by conducting a complete performance assessment and by simulating the electromagnetic signatures of lava tubes using a coherent 3D simulator.

The results show that radar sounding of lava tubes is feasible with good performance margins in terms of signal-to-noise and signal-to-clutter ratio, and that a dual-frequency radar sounder would be able to detect the majority of lunar lava tubes based on their potential dimension with some limitations for very small lava tubes having width smaller than 250 meters. The electromagnetic simulations show that lava tubes display an unique signature characterized by a signal phase inversion on the roof echo. The analysis is provided for different acquisition geometries with respect to the position of the sounded lava tube. This analysis confirms that orbiting multi-frequency radar sounder can detect and map in a reliable and unambiguous way the majority of Moon lava tubes.

Keywords: Moon Lava Tubes, Radar Sounder, Lunar Pits, Electromagnetic Signatures, Radar Simulations

1. Introduction

In the last years, there has been a renewed interest in the exploration of the Moon. Our satellite is a potential strategic outpost with significant raw materials reserves [1]. Lunar lava tubes are considered to be one of the main candidates for a future human outpost [2]. They are natural subsurface conduits which are the result of volcanic activity [3]. A lava tube is formed when the upper part of a given lava stream cools down and crusts while the lower part of it continues to flow, which results in the formation of an empty cave.

Moon lava tubes are considered to be important and useful structures since they can offer shelter against meteorite impacts, radiation [4] and strong thermal variations taking place on the Moon surface [2]. Recent studies based on gravity measurements [5, 6] and experimental evidence based on terrain mapping camera [7, 8] suggest the hypothesis that there is an abundance of lava tubes on the Moon and their dimensions are consistently larger than the ones found on the Earth. The main reason for their large size, is that the Moon gravity is considerably lower than the terrestrial one.

A complete map of the lava tubes dimension and location will provide important information in view of the exploration and colonization of the Moon. However, the mapping of lava tubes with optical camera has limitations. This is due to the fact that lava tubes are essentially subsurface structures. Radar observations at 70-cm wavelength of the region near Bessel crater in Mare Serenitatis show dark-radar lineaments. This can be interpeted as locally deeper regolith filling voids which might be collapsed portions of once subsurface lava tubes [9]. Unfortunately, radar waves at centimeter scale cannot penetrate through the regolith.

Planetary radar sounders instruments are low-frequency spaceborne ground penetrating radars which are particularly suitable for revealing the presence of lava tubes concealed under the Moon surface. Their signal wavelength is in the order of metres. These types of instruments are capable of transmitting pulsed electromagnetic energy and recording any reflection generated by dielectric discontinuities in the target terrain. In particular, by analysing the electromagnetic characteristic of the echo signals generated from both the Moon surface and subsurface, it is possible to understand the physical composition of the lava tube (*e.g.*, whether it is empty or not), its size and shape and the nature of the material forming the lava tube roof and floor.

Two radar sounding missions already probed the Moon surface, NASA's Apollo lunar radar sounder experiment (ALSE) and JAXA's LRS instrument onboard the Kaguya spacecraft [10, 11] but they were not specifically designed for lava tubes detection. Very recently, an intact lava tube was detected in the data acquired by the Lunar Radar Sounder (LRS) [12]. On the one hand, this confirms the potentiality of sounders to detect lava tubes, but on the other hand, LRS has not been specifically designed for the detecting them. Thus, due to its very low spatial resolution (due to a relatively small carrier frequency), it

can only detect very large lava tubes. A recent paper has nevertheless highlighted the possibility of detecting lava tubes of sub-resolution size (LRS resolution is 75m)[13]. However, in the paper there are two different interpretation of the lava tube detection results namely (i) the lava tube roof echo is buried in the surface response or (ii) the lava tube echo floor is buried in the roof radar echo. A dedicated, higher-frequency radar, however, would be able to make more conclusive detections of such small and shallow tubes, which are of special importance since they are easier to explore either by manned or unmanned missions.

Sood et al. [14] highlighted the scientific value of a radar sounder mission specifically designed for lava tubes detection. However, they did not provide an assessment analysis on how an hypothetical sounder system will be able to perform for this specific task and how to interpret the returning data. The studies performed on terrestrial lava tubes with ground penetrating radar [15, 16, 17] are of marginal relevance in terms of system design for the planetary radar sounding case. This is due to the very different acquisition geometry and very different radar system technological implementations.

This paper addresses the problem of detecting lava tubes on the Moon from orbit by using radar sounders. To this extent, the main goals of this paper are (i) the understanding of the design requirements that the sounding system should have for effective lava tube sounding, (ii) a performance assessment as function of the radar, geometric and terrain parameters and (iii) extensive simulations and analysis of the lunar lava tubes electromagnetic responses. The evaluation of the electromagnetic signatures is needed for providing a better understanding of the potential recorded data and thus greatly aiding its scientific interpretation. In our analysis, the allowed lava tube sizes are the ones provided in the recently published structural stability analysis based on gravity measurements presented by Blair et al. [5], which also envelopes the lava tube sizes provided by Coombs et al. [18].

The remainder of the paper is organized as following. Section 2 introduces the acquisition geometry and the subsurface structure assumptions. This serves as a basis for the performance analysis and lava tubes detectability results of Section 3. Section 4 presents the lava tubes electromagnetic signature analysis for different scenarios. Finally, Section 5 addresses the conclusions of this paper.

2. Radar Sounding Acquisition Geometry and Subsurface Structure Assumptions

In this section, we introduce the radar sounding geometry and the main assumptions regarding the Moon's lava tubes structure. This forms the basis for the next sections of the paper.

Let us consider a radar sensor with carrier frequency assumed to be in the range between 1 MHz to 100 MHz positioned at certain height h from the surface as shown in Fig. 1. We define a coordinate reference system composed by three orthogonal axes which are denoted as (i) along-track (*i.e.*, in the direction of the sensor movement), (ii) across-track (*i.e.*, in the direction orthogonal to the sensor movement) and (iii) height/depth direction (which is perpendicular to the other ones previously defined).

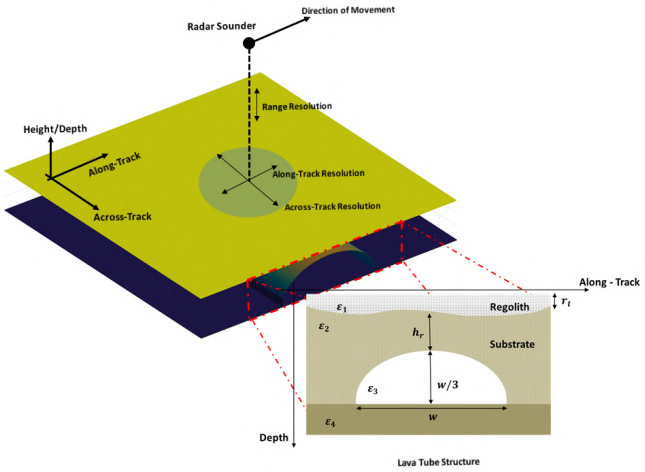

Figure 1: Radar sounder acquisition and terrain geometry

We consider the surface substrate to be covered by a regolith layer with average thickness denoted as r_t. We assume the base of the regolith (*i.e.*, the interface between the regolith and the substrate) to be rough. The slope of this rugged base is poorly constrained in the literature. The best piece of evidence available for estimating its order of magnitude (at least in Maria regions) is an optical image of the regolith base on Rima Hadley at Apollo 15 landing site [19] and the pit rims features exposing layered walls of basalt below the regolith [20]. Such optical clues suggest that the regolith base relief is in the order of metres. This is also suggested by the earth-based radar mapping observations at 70-cm wavelength scale [9]. Due to this uncertainty, we follow the same approach described in [21], where the base of the regolith roughness is assumed to be of the same magnitude as the one measured by the Lunar Orbiter Laser Altimeter (LOLA) [22]. A given lava tube is geometrically described by (i) its depth of the roof, denoted as h_r, (ii) its width, denoted as w, and (iii) its height, which is set equal to $w/3$. These assumptions are based on the structural analysis of Blair et al. [5]. The work by Coombs et al. [18] on lunar rilles suggests lava tubes of dimension far smaller than the possible maximum dimension specified by Blair et al.[5]. In any case, the numbers given in [18] are covered by the provided lava tube dimensions in [5] and therefore included in our analysis.

The length of a lava tube is not specified and it is assumed to be in the order of kilometres [2, 18]. For what pertains the surface and subsurface materials we denote as ϵ_1, ϵ_2 and ϵ_4 the real part of the dielectric constant of the regolith, the lava tube roof, and lava tube floor (*i.e.*, cave bottom), respectively. The dielectric constant of the cave interior ϵ_3 is assumed to be the one of vacuum and is thus equal to 1.

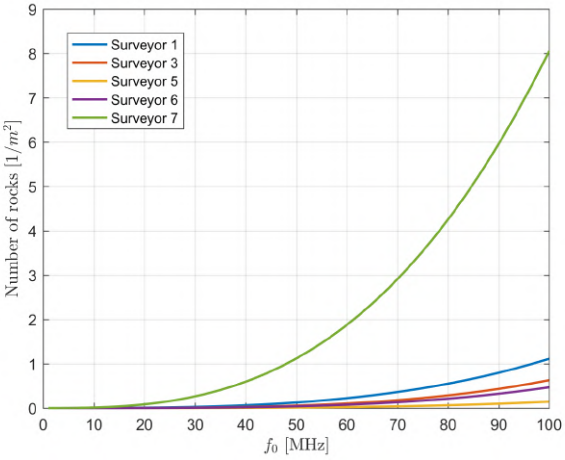

Figure 2: Number of rocks $[1/m^2]$ contributing to volume scattering as function of the carrier frequency f_0 and the Surveyor sampling site

3. Radar Sounder Design and Lava Tubes Detectability Analysis

In this section we study the requirements on the parameters of a radar sounder for detecting lava tubes and perform an analysis of the expected performances and detection capabilities. In Subsection 3.1, we assess the regolith contribution to echo power losses. Subsection 3.2 discusses the different resolution parameters. In subsection 3.3 the model for the echo power received by the lava tube is presented. Subsections 3.4 and 3.5 are devoted to the assessment of the signal-to-noise ratio (SNR) and signal-to-clutter ratio (SCR), respectively. Finally, Subsection 3.6 illustrates the results on the lava tube detectability by combining the analyses presented in the previous sections of this chapter. The final assessment provides information on whether a lava tube with given width and depth of the roof can be detected as a function of the probing central frequency.

3.1. Assessment on the Regolith Contribution to Echo Power Losses

Radar sounders propagation losses are classified in three different types namely (i) geometric losses due to the radial distance between the target and the sensor, (ii) attenuation losses induced by the terrain electric properties, and (iii) scattering losses due to heterogeneous inclusions in an otherwise homogeneous medium. In this section we investigate the impact of lunar regolith on both the attenuation and scattering losses, as well as on the dispersion of wide bandwidth waveforms.

Lunar surface is covered by a mantling layer composed of fragmented heterogeneous material denoted as regolith. Its average thickness is estimated to be 5 metres in Maria regions and 12 metres in Highland regions [23]. Being formed by an ensemble of objects (*e.g.*, rocks) of various sizes and shapes, they could potentially give rise to volume scattering phenomena. In general, for longer wavelength the scattering mechanism is dominated by the base of the regolith, whereas, for shorter ones, scattering on and within the regolith is an important factor contributing to losses [24]. Let us analyse a scenario of a regolith with thickness $r_t = 8.5$ m (*i.e.*, global average over the Moon surface) and rock inclusion modelled as dielectric spheres of radius comprised between $0.6\lambda/(2\pi\sqrt{\epsilon_1})$ and $10\lambda/(2\pi\sqrt{\epsilon_1})$ where $\epsilon_1 = 2.7$ is the average dielectric constant of the soil enclosing the rocks [23, 25] and λ the carrier frequency wavelength. According to Mie's theory [26], this particular range of radius size is the one that gives the highest backscattering values and, in turn, the greatest losses (*i.e.*, less electromagnetic energy propagates below the regolith).

We assume the volume rock population $N(d_r)[1/m^4]$ as function of the rock diameter d_r to be the one that has been measured by the Surveyor missions [24]. The number of rocks by unit area is equal to [24]:

$$N_r = r_t \int_{0.6\lambda/(\pi\sqrt{\epsilon_1})}^{10\lambda/(\pi\sqrt{\epsilon_1})} N(d_r)\, dd_r. \tag{1}$$

From the results reported on Fig. 2 we can infer that, even in a worst case scenario, the number of rocks comprised in the regolith by unit area having a size comparable to the incident wavelength is negligible over the entire frequency range of interest typical of radar sounding. The only exception to the general trend of Fig. 2 is the one inferred from Surveyor 7 data, which highlights marginal volume scattering effects for sounding frequencies higher than 80 MHz. However, recent discoveries suggest that the highest concentration of lava tubes lies in the Mare regions [20, 8]. The Surveyor 7 sampling site was located in the Highland plains region near Tycho crater, thus, in our case, of less significance when compared to Mare regions data where all the other Surveyor sampling sites were located.

Another potential contribution to echo power loss results from voids inclusion in the regolith material. The Maxwell-Garnett mixing model describes dielectric constant of the solid/pore filling mixture ϵ_m at different depths in the following way [27]:

$$\epsilon_m(z) = \epsilon_1 \frac{1 + 2\Omega(z)\xi}{1 - \Omega(z)\xi} \tag{2}$$

$$\xi = \frac{\epsilon_i - \epsilon_1}{\epsilon_i + 2\epsilon_1} \tag{3}$$

where ϵ_i is the dielectric constant of the inclusion assumed to be vacuum (i.e. $\epsilon_i = 1$). The model of the decline of porosity Ω as function of the depth z due to the lithostatic pressure is equal to [28]:

$$\Omega(z) = \Omega(0)e^{-z/K} \tag{4}$$

where $\Omega(0)$ is the surface porosity and K is a decay constant. $\Omega(z)$ and $\Omega(0)$ are porosity percentage divided by 100. The decay constant for the Moon is equal to $K = 6.5$ Km [28]. In this case, the two-way transmission coefficient between the regolith and the substrate T_{reg} is equal to;

$$T_{reg}(z) = (1 - \Gamma_{reg}^2(z))^2 \tag{5}$$

where Γ_{reg} is the porous base of the regolith reflection coefficient defined as:

$$\Gamma_{reg}(z) = \frac{1 - \sqrt{\epsilon_2/\epsilon_m(z)}}{1 + \sqrt{\epsilon_2/\epsilon_m(z)}} \tag{6}$$

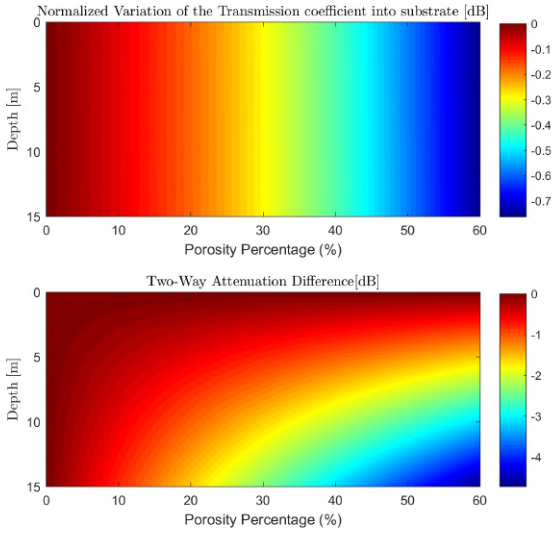

Figure 3: Example of normalized variation of the transmission coefficient and attenuation as function versus the regolith porosity percentage, $\epsilon_i = 1$, $\epsilon_1 = 4$, $\epsilon_2 = 8$, $\tan\delta = 0.03$, $f_0 = 100$ MHz

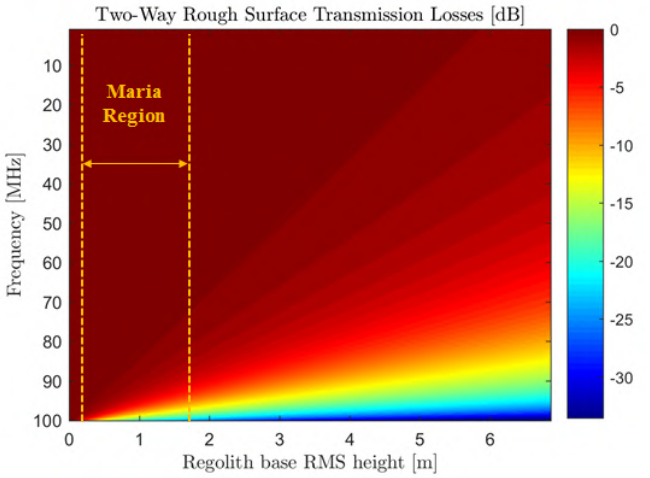

Figure 4: Two-Way rough surface transmission losses with respect to specular return induced by the regolith base as function of both its RMS variation of the height and the central frequency. Due to lack of knowledge regarding the roughness of the regolith base, range of plausible RMS height values for the Maria Region were calculated assuming that the base of the regolith roughness is of the same magnitude as that of the lunar surface which is constrained by LOLA [22]. In this example, the value of the substrate dielectric constant is assumed equal to $\epsilon_2 = 6$.

The real part of the permittivity and the loss tangent decrease when increasing the porosity. This implies that the reflection coefficient $\Gamma_{reg}(z)$ increases or decreases with the porosity depending on the value of ϵ_1 and ϵ_2. By assuming $2.5 \leq \epsilon_1 \leq 4$ and $4 \leq \epsilon_2 \leq 8$ [23, 25], the resulting decrease or increase of the transmission coefficient T_{reg} is smaller than 1 dB and thus negligible. The total two-way radar signal attenuation $L_{reg} = 0.18\sqrt{\epsilon_m(z)}\ \tan\delta\ z\ [dB/MHz]$ [29], where $\tan\delta$ is the loss tangent, decreases as function of the porosity and the depth. Its variation can be considered negligible at low frequencies (*e.g.*, 10 MHz). At 100 MHz, considering worst case parameters, there is a reduction in total signal attenuation up to 5dB as shown in Fig. 3). The values assumed for the loss tangent (i.e. 0.01 to 0.03) are in the upper range of the ones measured for the Moon basaltic material in our frequency range [30] and thus should be considered as worst case.

The waveform dispersion in the regolith is related to the frequency dependence of ϵ_1 and $\tan\delta$. If the phase of the signal is a linear function of frequency (*i.e.*, linear phase condition), there is no dispersion (i.e. temporal smearing) of the radar signal and thus no distortion. In the frequency range 1 MHz to 100 MHz, the tangent loss is always much smaller than one [31] and the real part of the dielectric constant has very small variations with frequency [31]. Under this assumptions of low-loss dielectric [26], linear phase condition of the signal in the regolith is met and thus there is no waveform dispersion.

According to the above analysis, we consider volume scattering, voids inclusions and signal phase dispersion effects negligible and thus in the following we will only take into account the regolith geometric and attenuation losses.

3.2. Resolution

Radar sounder capability of discriminating different targets is expressed by three different quantities namely along-track, across-track and range resolution. The radar range resolution is equal to:

$$R_r = \frac{c_0}{2B\sqrt{\epsilon_2}} = \frac{c_0}{f_0\sqrt{\epsilon_2}}, \tag{7}$$

where f_0 is the radar carrier frequency and c_0 the speed of the light. In this paper we assume 50% fractional bandwidth such that $B = 0.5 f_0$, which is reflected in the final derivation of equation (7). The rationale behind our assumption on signal bandwidth is that it is very difficult to synthesize very high fractional bandwidths from the technological point of view. This assumption allows to develop our analysis only in terms of the central frequency of the radar without loss of generality. For this application, the relevant medium for resolution computation is the one composing the lava tube roof (*i.e.*, the medium denoted as substrate in Fig. 1). The range resolution is typically in the order of metres. The along-track resolution is computed as:

$$R_{at} = \frac{\lambda h}{2L_s}. \tag{8}$$

We assume the length of the synthetic aperture equal to $L_s = \sqrt{\lambda h/2}$ [26], which corresponds to a resolution equal to $R_{at} = \sqrt{\lambda h/2}$. The signal wavelength is defined as $\lambda = c_0/f_0$ and h is the spacecraft height. Usually, the along-track resolution is in the order of hundred metres. The across track resolution is equal to the pulse-limited diameter [32]:

$$R_{act} = 2\sqrt{c_0 h/B}. \tag{9}$$

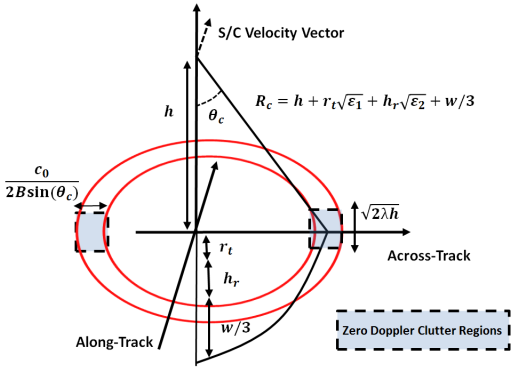

Figure 5: Illustration of the Clutter Geometry

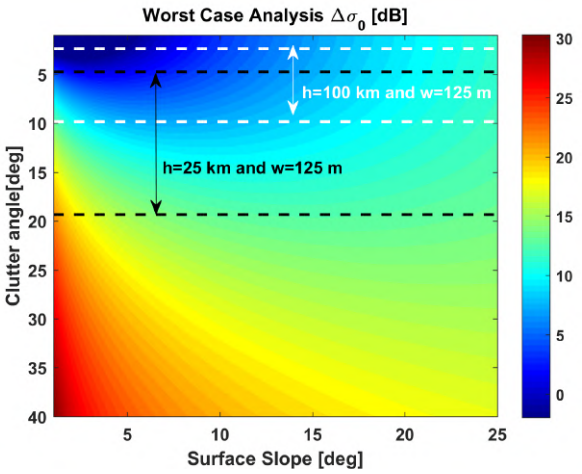

Figure 6: Worst case analysis for the back-scattering ratio $\Delta\sigma_0 = \sigma^0_f(0)/\sigma^0_s(\theta_c)$ [dB] between the subsurface and surface versus the clutter angle θ_c and the surface RMS slope s. The dashed lines are constraining the values of the clutter angle θ_c as function of the S/C height h, the lava tube roof h_r and the lava tube width w. The analysis is performed for the lava tube of width $w = 125$ which is the one resulting in the smallest clutter angles thus considered worst case.

The across-track resolution is the main limitation of a radar sounder. Its large value is dictated by the fact that, for mechanical reasons, a dipole antenna is usually deployed, resulting in a very large footprint. The large dimensions of the footprint combined with the fact that no synthetic aperture can be formed in the direction perpendicular to the S/C motion, results in an across-track resolution in the order of thousand metres.

3.3. Lava Tube Floor Echo Power

The radar echoes of interests are those arising from the lava tube roof and floor. The radar echo undergoing the most attenuation is the one generated by the lava tube floor. Accordingly, we model the echo power received from it as function of the radar and surface/subsurface parameters. The echo power density S_i $[W/m^2]$ measured at the radar antenna (without considering the terrain attenuation and backscattering) is equal to:

$$S_1 = \frac{P_t G^2 \lambda^2}{(4\pi)^3 R_e^4}, \tag{10}$$

where P_t is the radar transmitted power, G the antenna gain and R_e the effective radar distance to the target, which is equal to:

$$R_e = h + r_t/\sqrt{\epsilon_1} + h_r/\sqrt{\epsilon_2} + w/3. \tag{11}$$

The effective radar distance is the one from the radar to the floor of the lava tube and it depends on the regolith depth r_t, the depth of lava tube roof h_r and the lava tube height (which is assumed equal to $w/3$, where w is the width of the lava tube). The effective distance is reduced in both the regolith and lava tube roof medium according to the decrease in velocity of the electromagnetic wave.

The echo power density S_i is reduced by the two-way attenuation the transmitted pulse experiences as it travels through both the regolith and lava tube roof such that:

$$S_2 = S_1 e^{-2\alpha f_0(\sqrt{\epsilon_2}h_r + \sqrt{\epsilon_1}r_t)}, \tag{12}$$

where $\alpha = 2\pi/c_0 \tan\delta$ is the two-way attenuation constant. We assume the loss tangent $\tan\delta$ to be equal for both the regolith and the lava tube roof.

At each interface (*i.e.*, dielectric contrast between different materials) part of the energy is reflected toward the radar and part of it continues to travel downwards into the target terrain. Therefore the power density S_2 is further reduced by the various interfaces reflections such that:

$$S_3 = S_2\, T^2_{01}\rho_{12}T^2_{12}T^2_{23}, \tag{13}$$

where the transmission coefficient T_{ij} between the i-th and j-th medium is equal to $T_{ij} = 1 - \Gamma_{ij}$.The Fresnel power reflection coefficient at normal incidence denoted as Γ_{ij} defined as follows:

$$\Gamma_{ij} = \left|\frac{1 - \sqrt{\epsilon_j/\epsilon_i}}{1 + \sqrt{\epsilon_j/\epsilon_i}}\right|^2. \tag{14}$$

The transmission factors are related to the vacuum-regolith, regolith-roof and roof-cave interfaces.
The regolith-roof interface is the one between the regolith and the substrate.
As discussed in Section 2, this interface is rough. Accordingly, let ρ_{12} be the two-way rough surface transmission power loss with respect to the specular return [33, 34, 35]:

$$\rho_{12} = J_0^2(\frac{\psi^2}{2})e^{-\psi^2} \tag{15}$$

where $J_0(.)$ is the zero-order modified Bessel function and ψ is the RMS phase variation induced by the rough surface on the transmitted signal which is equal to:

$$\psi = \frac{4\pi\sigma_b}{\lambda}(\sqrt{\epsilon_2} - 1) \tag{16}$$

The RMS variation of surface height σ_b is referred to the base of the regolith. As already stated in Section 2, the base of the regolith roughness is assumed to be of the same magnitude as

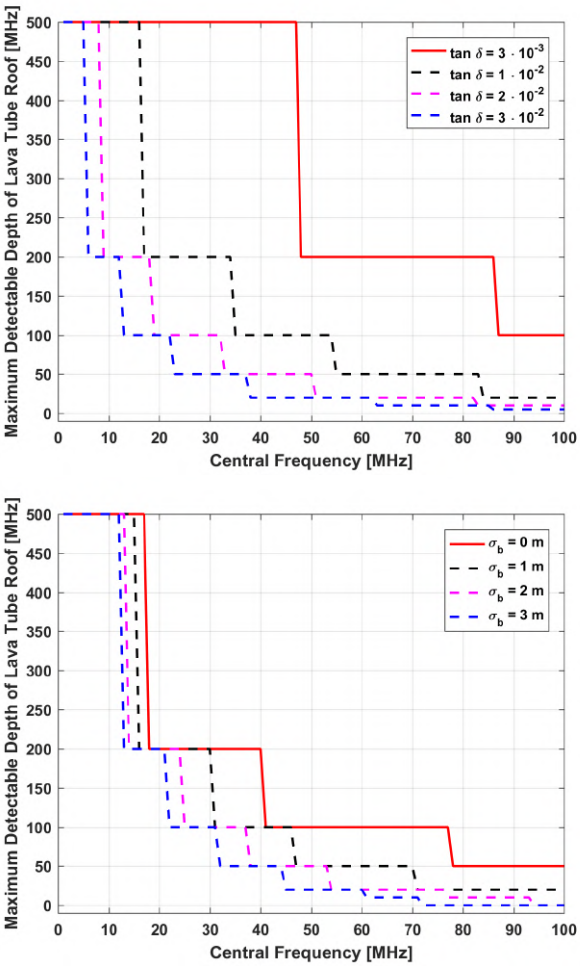

Figure 7: (a) Maximum detectable depth of lava tube roof h_r versus the carrier frequency f_0 for different values of (a) loss tangent and (b) basalt substrate RMS variation of surface heights. The depth of lava tube roof is discretized according to the structural stability matrix of [5].

that measured by LOLA [22]. Accordingly, we constrain the average value of σ_b to 0.6 m by considering the average range of slope values for the Maria region provided in [22].
To retrieve the lava tube floor echo power P_f $[W]$, the power density S_3 is multiplied by radar cross-section of the lava tube floor as follows:

$$P_f = S_3\, \sigma_f^0(0) A_f, \tag{17}$$

where $A_f = \min\{w, \sqrt{2\lambda h}\} \cdot \sqrt{2\lambda h}$ is the equivalent area of the lava tube floor. If the lava tube width is greater than the first Fresnel diameter, we consider a rectangular area formed by the latter. The length of the lava tube is assumed to be in the order of kilometres [2], thus it is appropriate to consider only the contribution of the coherent part of the scattered field given by the first Fresnel diameter. We denote as $\sigma_f^0(0)$ the backscattering cross-section normalized to unit area defined as follows [36]:

$$\sigma_f^0(\theta) = \frac{C_f \Gamma_{34}}{2} \frac{1}{[\cos^4(\theta) + C_f \sin^2(\theta)]^{3/2}}. \tag{18}$$

Hagfor's model is particularly appropriate because it has been already applied and validated on Moon data. The value of the constant $C_f = 1/s_f^2$ can be computed assuming the reference slope to be equal to $s_f = tan^{-1}(\frac{\sigma_f}{w})$. There is no available data regarding the rms value of the floor height distribution σ_f. We know from terrestrial lava tubes that the floor relief can vary from relatively smooth to very rough and knobby [2]. Moreover, this variability occurs at scales considerably smaller than the lava tube cross-sectional dimension. Assuming that the tube height is equal to $w/3$, and assuming a Gaussian distribution for the floor height variation inside the lava tube, we can safely constraint the rms height such that $4\sigma_f = w/3$. This, in turn, provides the value of the reference slope assumed equal to $s_f = \tan^{-1}(\frac{1}{12}) = 0.0831$ rad.

3.4. Signal to Noise Ratio (SNR)

The signal-to-noise ratio is expressed with reference to the power scattered by the floor of the lava tube as follows [32]:

$$SNR = \frac{P_f}{P_n} = \frac{P_t G^2 \lambda^2 \sigma_f^0(0) A_f}{(4\pi)^3 (h + r_t + h_r/\sqrt{\epsilon_1} + w/3)^4} \frac{T_{01}^2 \rho_{12} T_{12}^2 T_{23}^2 e^{-2\alpha f_0 (\sqrt{\epsilon_2} h_r + \sqrt{\epsilon_1} r_t)}}{k_b T_e(f_0) B}, \tag{19}$$

where the noise power is equal to $P_n = k_b T_e(f_0) B$, k_b is the Boltzmann constant and $T_e(f_0)$ is the frequency dependent galactic noise temperature[37]. It is clear from equation (19) that the attenuation term and, in turn, the depth of lava tube roof h_r play a major role in the SNR performance of the radar system. Another important factor affecting the SNR is the two-way rough surface transmission term $\rho_{12} \sim e^{-f_0^2}$. Indeed, the analysis of the two-way rough surface transmission losses ρ_{12} of equation (15) shows that the frequency range 80 MHz to 100 MHz is particularly affected by the roughness of the base of the regolith in the Maria region (see Fig. 4).
The range compression gain is equal to

$$G_r = B \cdot T_s, \tag{20}$$

where T_s is the transmitted pulse width. The azimuth compression gain is equal to

$$G_{az} = \frac{L_s}{v_s\, PRI} = \frac{\sqrt{2\lambda h}}{v_s} PRF, \tag{21}$$

where $PRF = \frac{4 v_s}{\lambda} \sin\theta_c$ is the minimum pulse repetition frequency of the radar required for sampling the Doppler spectrum, and v_s is the orbital velocity. For the definition of the clutter angle θ_c the reader can refer to the next section.

3.5. Clutter Model and Signa-to-Clutter Ratio (SCR)

In radar sounding, clutter is defined as off-nadir echoes coming from the surface which may mask the echoes of interest coming from the subsurface. This generates ambiguities and may hinder data interpretation. The clutter slant range (see Fig. 5) with respect to the lava tube floor is equal to:

$$R_c = h + r_t \sqrt{\epsilon_1} + h_r \sqrt{\epsilon_2} + w/3. \tag{22}$$

As a result of the azimuth radar focusing, the equivalent clutter area is given by [38]:

$$A_c = \sqrt{2\lambda h}\frac{c_0}{B\sin(\theta_c)}. \quad (23)$$

This area corresponds to the one such that the illuminated points have zero Doppler. The clutter angle θ_c is equal to

$$\theta_c = \cos^{-1}(h/R_c). \quad (24)$$

The clutter echo power P_c is equal to

$$P_c = \frac{P_t G^2 \lambda^2 \sigma_s^0(\theta_c) A_c}{(4\pi)^3 R_c^4}, \quad (25)$$

where the surface back-scattering coefficient is expressed as for the Hagfor's model:

$$\sigma_s^0(\theta) = \frac{C_s \Gamma_{01}}{2}\frac{1}{[\cos^4(\theta) + C_s \sin^2(\theta)]^{3/2}}, \quad (26)$$

where $C_s = 1/s(\lambda)^2$ and $s(\lambda) = s_0\,(\lambda/\lambda_0)^{H-1}$ is the frequency dependent RMS slope of the surface [39], H is the surface Hurst exponent and s_0 the reference RMS slope. The reference wavelength and slopes are assumed equal to $\lambda_0 = 17$ m and $s_0 \leq 25$ deg respectively [22]. The value of the Hurst exponent can be assumed in the range $0.7 \leq H \leq 1$ [22]. The signal to clutter ratio denoted as SCR is defined as:

$$SCR = \frac{P_f}{P_c} = \left(\frac{h + r_t\sqrt{\epsilon_1} + h_r\sqrt{\epsilon_2} + w/3}{h + r_t/\sqrt{\epsilon_1} + h_r/\sqrt{\epsilon_2} + w/3}\right)^4 \frac{\sigma_f^0(0)}{\sigma_s^0(\theta_c)} \\ T_{01}^2 \rho_{12} T_{12}^2 T_{23}^2 \frac{A_f}{A_c} e^{-2\alpha f_0(\sqrt{\epsilon_2}h_r + \sqrt{\epsilon_1}r_t)}. \quad (27)$$

The dominant parameters which mainly drive the value of the SCR are the clutter angle θ_c (which controls the value of σ_0), the attenuation terms $e^{-2\alpha f_0\sqrt{\epsilon_2}h_r}$ and $\rho_{12} \sim e^{-f_0^2}$. For a fixed f_0, the sounding of large lava tubes (in terms of width) is less affected by clutter when compared to small lava tubes. As w increases (note that the lava tube height is assumed equal to $w/3$), the clutter angle increases and thus σ_s^0 decreases. This results in an improvement of the SCR. Another factor affecting SCR is the sensor height h. By lowering it, the SCR increases due to the direct increase of θ_c.

In equation (27) the most difficult term to analyse is the one accounting for the surface and subsurface backscattering, which we denote as $\Delta\sigma_0 = \sigma_f^0(0)/\sigma_s^0(\theta_c)$.

Assuming a worst case scenario such that $\epsilon_2 = 8$ and $\epsilon_3 = 4$, Fig. 6 shows that, even if for small surface slopes and small clutter angles θ_c, the clutter backscattering contribution (*i.e.*, σ_s^0) does not considerably degrade the SCR performance. Therefore we can conclude that the dominant factor for SCR degradation is the subsurface attenuation and the relief at the base of the regolith.

3.6. Lava Tubes Detectability

The analyses presented in sections 3.4 and 3.5 highlight that the main driving factor affecting the radar performance is the substrate attenuation on the radar signal which mainly depends on the depth of the lava tube roof h_r, the central frequency f_0 and the RMS variation of surface heights of the regolith-substrate interface σ_b for fixed subsurface properties in terms of complex dielectric constant. The lava tube width w plays a secondary role in terms of SCR and SNR when compared to the depth of lava tube roof.

Fig. 7 shows the maximum depth at which a lava tube can be detected for different carrier frequencies as function of $\tan\delta$ and σ_b. As expected, the maximum detectable depth of the lava tube roof is strongly dependent on f_0. Fig. 7 (b) shows that the base of the regolith roughness strongly impacts performance in the range 80 MHz to 100 MHz.

Performances have been evaluated considering radar system parameters based on previous Moon radar sounding missions [11]. Accordingly, the transmitted power is set equal to $P_t = 800$ W, the antenna gain is equal to $G = 1$ dB, the pulse repetition frequency $PRF = 500$ Hz, the pulse width $T_s = 100\,\mu$s and the S/C height equal to $h = 25$ km. For what regards the Moon surface parameters, we assume a representative and rather challenging scenario, from the attenuation point of view, such that $H = 0.8$, $s_0 = 2.5$ deg, $\epsilon_1 = 2.7$, $\epsilon_2 = 4$, $\epsilon_4 = 4$, $\tan\delta = 0.01$, $r_t = 8.5$ m and $\sigma_b = 0.6$ m. These values are in line with what discussed in the previous section of the paper [23, 25, 22]. The rest of the parameters described in Section 3.2 - 3.5 are derived from the ones listed above. Fig. 8 shows the results regarding SNR, SCR and detection matrix for three different carrier frequencies namely 10 MHz, 50 MHz and 100 MHz. The detection matrix is displayed in the same fashion as the structural stability one presented in [5]. The lava tubes dimension we consider feasible and for which detectability is provided are the stable and quasi-stable configurations for both the lithostatic and Poisson stress state in the material models as in [5]. Accordingly, performance for unstable lava tubes were not computed.

A lava-tube is considered detectable if, for a specific combination of lava tube roof depth h_r and lava tube width w, all of the following conditions holds true: (i) $SCR > 0$ (ii) $SNR > 10$ dB, (iii) h_r greater than two times the range resolution defined as in Section 3.2, (iv) w greater than the along-track resolution defined as in Section 3.2. It is clear from Fig. 8 that for $f_0 = 10$ MHz only very large lava tubes can detected. These large lava tubes are detected with very solid performances in terms of SNR. On the other hand, for a frequency $f_0 = 100$ MHz, small lava tubes can be detected and with a lower SNR when compared to the 10 MHz sounding case. Finally, the $f_0 = 50$ MHz sounding frequency is suitable for detecting medium size lava tubes. Therefore there is a clear correlation between the sounding central frequency and the dimension of the lava tubes that can be detected with it.

By further analysing the results of Fig. 8 we can highlight a general scheme in terms of lava tubes detection as function of their width w and lava tube roof depth h_r. With reference to Fig. 9, the area of feasible lava tube detection presented in blue is constrained by three different sub-bands. Each sub-band thickness depends on certain radar performance factors which are mainly affected by the selected radar central frequency f_0.

On the basis of this analysis, we can concluded that given

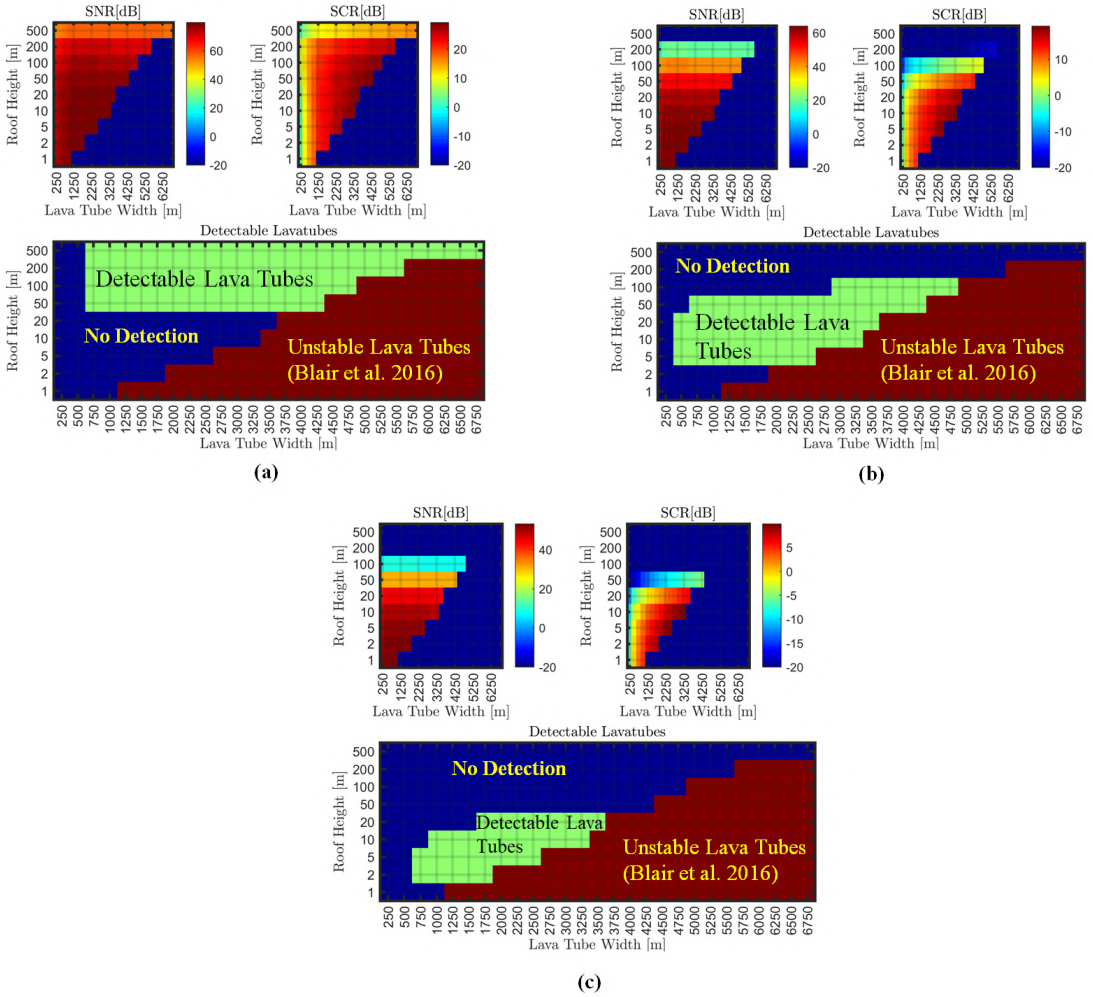

Figure 8: SNR, SCR and detectability matrix for (a) f_0 = 10 MHz (b) f_0 = 50 MHz and (c) f_0 = 100 MHz assuming loss tangent equal to $\tan\delta = 0.01$ and RMS height variation of basalt substrate equal to $\sigma_b = 0.6$ m.

the expected dimension of lava tubes, a multi-frequency radar sounder will allow to map the majority of them with some detection limitations for lava tubes having width smaller than 250 m. This can be done by selecting at least two frequencies, one from the lower and one from the upper part of the 1 to 100 MHz frequency range. As an example, Fig. 10 shows that a radar sounder with lower carrier frequency equal to 10 MHz and higher one of 100 MHz is potentially able to detect the vast majority of the allowed (in terms of structural stability) lava tubes sizes if $\tan\delta = 0.01$. However, to take margin against the basalt surface relief and loss tangent variation that have a major impact on performance (see Fig. 7 (b)), a central frequency in the range 60 to 65 MHz is a better tradeoff choice (see Fig. 10 (c)) for detecting small lava tubes under the 50 % fractional bandwidth assumption.

4. Lava Tubes Electromagnetic Signatures

This section is devoted to the analysis of the electromagnetic signature of lava tubes of different dimensions, in the frequency range of 1 MHz to 100 MHz identified in the previous section. We investigate the radar returns resulting from a range of lava tubes geometries using of a multi-layer coherent simulator. Lava tubes echoes are generated for different radar central frequencies and different crossing angles assuming to transmit with a linear chirp weighted by an Hann window. Range-compression is then applied to the simulated data. The crossing angle is defined as the angle at which the spacecraft ground trace intersects the line perpendicular to the lava tube axis. The coherent simulator allows us to analyse both the received signals power and the phase information.

Although the simulator works with interfaces represented by 3D surfaces, it is possible to simulate 3D volumes by cladding two properly-chosen surfaces together, as shown in Fig. 11. Lava tubes are modelled in this fashion, where one surface containing an open half-cylinder is clad to a flat surface underneath, thus adding a ground to the lava tube. It is worth noting that a minor issue arises when modelling the tubes this way. Because the simulator processes the subsurface layers in an iterative way, a reflection is generated by the layer containing the

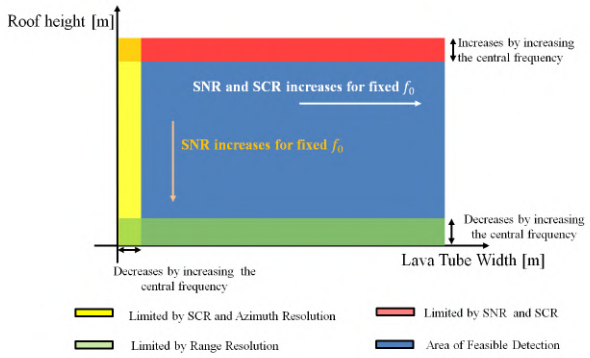

Figure 9: General scheme of lava tube detection versus the lava tube width and the depth of lava tube roof. The area of feasible lava tube detection is depicted in blue. The size of this area is bounded by three smaller sub-bands which size depends on the value of the radar parameters. The radar central frequency is the main factor affecting the size of these sub-bands.

open half-cylinder, but this feature is easily recognizable in the resulting radargram and does not endanger the general picture of the simulation. For what pertains the subsurface geoelectrical properties, we assume the medium between the lunar surface and the lava tube roof to be basalt with real part of the dielectric constant equal to $\epsilon_{r,1} = 4$ and loss tangent equal to $\tan\delta_1 = 0.01$. The lava tube floor is described by a dielectric constant equal to $\epsilon_{r,3} = 4$. We consider the space between the lava tube roof and floor as empty such that $\epsilon_{r,2} = 1$. The rest of this section is organized as follows. In section 4.1 we investigate the electromagnetic signature of lava tubes of different sizes assuming an ideal geometry such that the lunar surface is flat and the lava tubes are modelled with perfect geometric shapes. This is done in order to establish clear reference cases for the lava tubes electromagnetic responses. Then, in section 4.2, we present simulations of more realistic scenarios. This is done by modelling irregular lava tubes and a lunar surface characterized by the presence of craters and significant roughness.

4.1. Lava Tubes Electromagnetic Signatures : Ideal Geometry

We investigated four lava tubes of different sizes selected on the basis on the structural stability analysis of [5]. The simulations on the selected cases where performed at two different combinations of central frequencies and bandwidths : (i) $f_{0,1} = 10$ MHz and a bandwidth $B_1 = 5$ MHz, and (ii) $f_{0,2} = 60$ MHz and $B_2 = 30$ MHz. The simulations were performed for the following four scenarios : (a) perpendicular (to the lava tube axis), (b) centred parallel, (c) off-centre parallel, and (d) oblique with an angle of 45°, all of which are represented schematically in Fig. 11. The radar altitude was set to $h = 100$ km for all runs, and the radar peak power to $P = 800$ W. The footprints considered have a radius equal to twice the pulse-limited zone radius of each instrument, that is, $A_1 = 4897$ m and $A_2 = 1999$ m. The investigated cases, covering different lava tubes sizes, are summarized in Table 1.

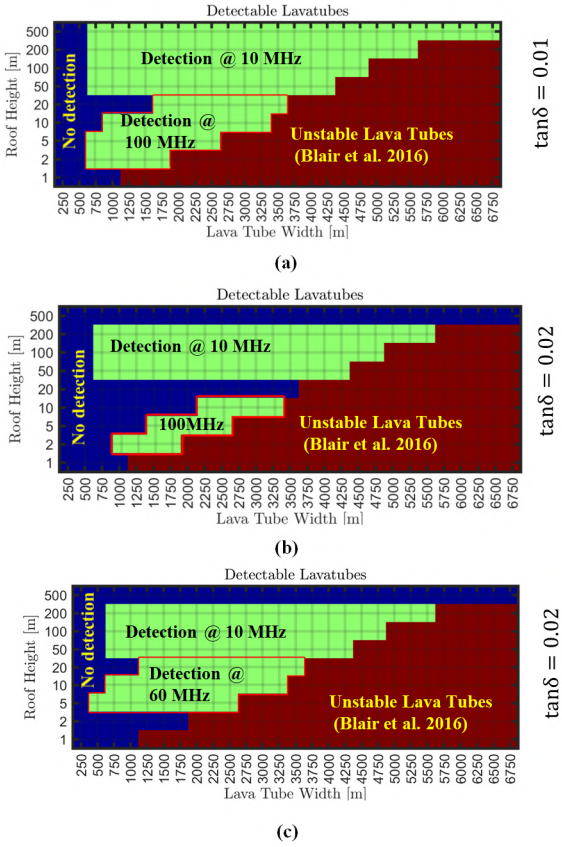

Figure 10: Examples of detectable lava tubes by combining the sounding at two different carrier frequencies. (a) $\tan\delta = 0.01$, $\sigma_b = 0.6$ m, lower frequency equal to 10 MHz, higher frequency equal to 100 MHz (b) $\tan\delta = 0.02$, $\sigma_b = 0.6$, lower frequency equal to 10 MHz, higher frequency equal to 100 MHz (c) $\tan\delta = 0.02$, $\sigma_b = 0.6$ m, lower frequency equal to 10 MHz, higher frequency equal to 60 MHz.

In order to establish a series of clear reference cases, the lava tubes are modelled with perfect linearity and curvature. The lunar surface is modelled as flat. To avoid ray-tracing artifacts, some minimal roughness was added to every interface by adding a surface modelled as fractional Brownian motion with a Hurst's coefficient $H = 0.1$ and a topothesy $T = 0.26$ m.

Experimental results show that the lava tubes signatures for the parallel and oblique crossing cases are composed of two vertically-aligned ensembles of hyperbolas (see Fig. 12). The upper and lower features correspond to the lava tube roof and the floor, respectively. The two hyperbolas brightness is similar. The finer characteristics of these signatures strongly depend on the probing central frequency and associated bandwidth. For lava tubes sounded with the 60 MHz radar, the signatures are clearer and reduce to two simple hyperbolas corresponding to the roof and to the floor (see Fig. 14-left). For the 10 MHz central frequency case, each of the two traces is rather made of one bright hyperbola and some dimmer, more chaotic echoes underneath as shown, for example, in Fig. 12. We interpret the brighter hyperbola of the upper trace as generated by the

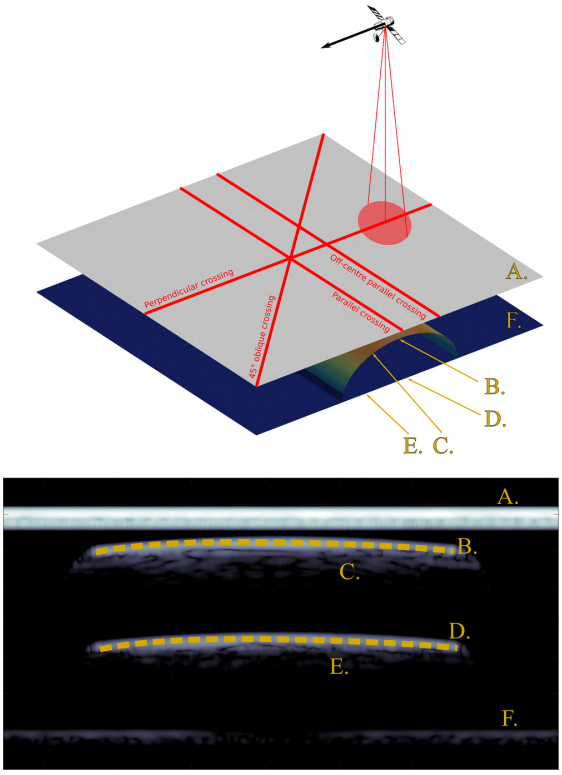

Figure 11: Illustration of the different acquisition geometries considered in the simulations (top), along with an example of simulated radargram for a perpendicular crossing direction (bottom), where key features of the terrain are cross-references with features on the radargram : A. surface, B. tube apex, C. tube walls, D. central portion of the floor, E. remainder of the floor, F. parasitic subsurface resulting from the terrain modelling (disregarded in the analysis).

apex of the tube (the centre of the floor for the lower part of the signature), and the more random pattern beneath it, from the tube walls (from off-nadir floor portions). These diffuse radar returns are less prevalent in the 60 MHz radar case due to the higher subsurface attenuation. The above-mentioned features are summarized in Fig. 11.

The only noticeable difference between the two crossing scenarios is that the features are spatially more stretched in the oblique crossing case when compared to the parallel one (see Fig. 12). The stretching factor is equal to $\cos\theta^{-1}$, where θ is the angle between the spacecraft ground trace direction and the line perpendicular to the lava tube axis.

In the parallel crossing case, the roof and floor appear as two parallel lines (see Figs. 13 and 14-right). Similarly to the previous case, there are some diffuse spurious reflections, which are more prominent in the 10 MHz case. The 60 MHz radargrams displays two clearer lines, as those off-nadir subsurface echoes are more strongly attenuated than in the 10 MHz case. There are no significant differences between a centred crossing and an off-centre crossing except from a slight variation of the relative power levels of the tube and floor echoes (see Fig. 13).

Our simulations highlight the very important feature of phase inversion, which can be observed in the radargrams of every detectable tube irrespective of the crossing direction (see Figs. 12, 13, and 14). Indeed, the roof echo presents a 180° phase

Tube Size	Width [m]	Height [m]	Roof depth [m]
Very Large	4000	1333	200
Large	3000	1000	20
Medium	1250	416	50
Small	500	167	20

Table 1: Dimensions of the four cases of lava tubes analysed in this study. Tube height is always equal to one-third of the tube diameter according to the stability analysis of [5]

shift with respect to the surface echo. This is expected from a wave traveling from a medium 1 to a medium 2 characterized by $\epsilon_1 > \epsilon_2$ (*i.e.*, roof medium to vacuum interface).
To retrieve the subsurface phase component resulting from the interface reflection, the path-length phase contribution should be subtracted from the overall echo signal phase. In our simulations, we can perform this compensation in a deterministic way since we can exploit the *a-priori* information in the digital elevation model. In practice, phase inversion resulting from the interface reflection can be separated from the phase change due to path-length difference in a similar fashion as it is performed in ground penetrating radar (GPR) phase-based techniques for ground profiling [40, 41, 42, 43]. Radar sounder illuminates wider surface areas with respect to GPR, therefore the surface topography phase contribution shall be taken into account when compensating for the path length. Fortunately, high resolution DEM of the Moon are available, thus both clutter returns detection [44] and subsequent topography phase contribution correction can be performed if needed.
Another important issue is the phase noise induced by the galactic noise. To address this issue, we performed Monte Carlo simulations (about 5000 trials for each step of SNR) by injecting random gaussian noise into the signal and computing the absolute phase error induced by the noise. The simulations of Fig. 17 show that with an SNR equal or greater than 10 dB the absolute phase error can be considered acceptable. As it will be presented in the next subsection, phase inversion is a key feature for the differentiation of legitimate lava tubes echoes from the ones generated by off-nadir surface clutter.

The simulated electromagnetic signatures largely confirmed the conclusions of the performance analysis. Large lava tubes buried several hundreds of metres below the surface were only visible in the radargram with the 10 MHz carrier frequency instrument. On the other hand, the detection of shallow lava tubes was unambiguous only with the 60 MHz radar. On a few cases related to very shallow lava tubes, discrepancies appear between the simulation and the performance analysis. For instance, the upper hyperbola of the $w = 1250\,\text{m}$, $h_r = 50\,\text{m}$ lava tube cannot be distinguished from the surface response using the 10MHz radar. This is due to the fact that the range resolution computation does not take into account the elongation of the surface response over many range cells. Accordingly, the radar echoes originating from the roof of very shallow lava tubes may be buried in the surface echo. This depends on the lunar surface and radar antenna characteristics.

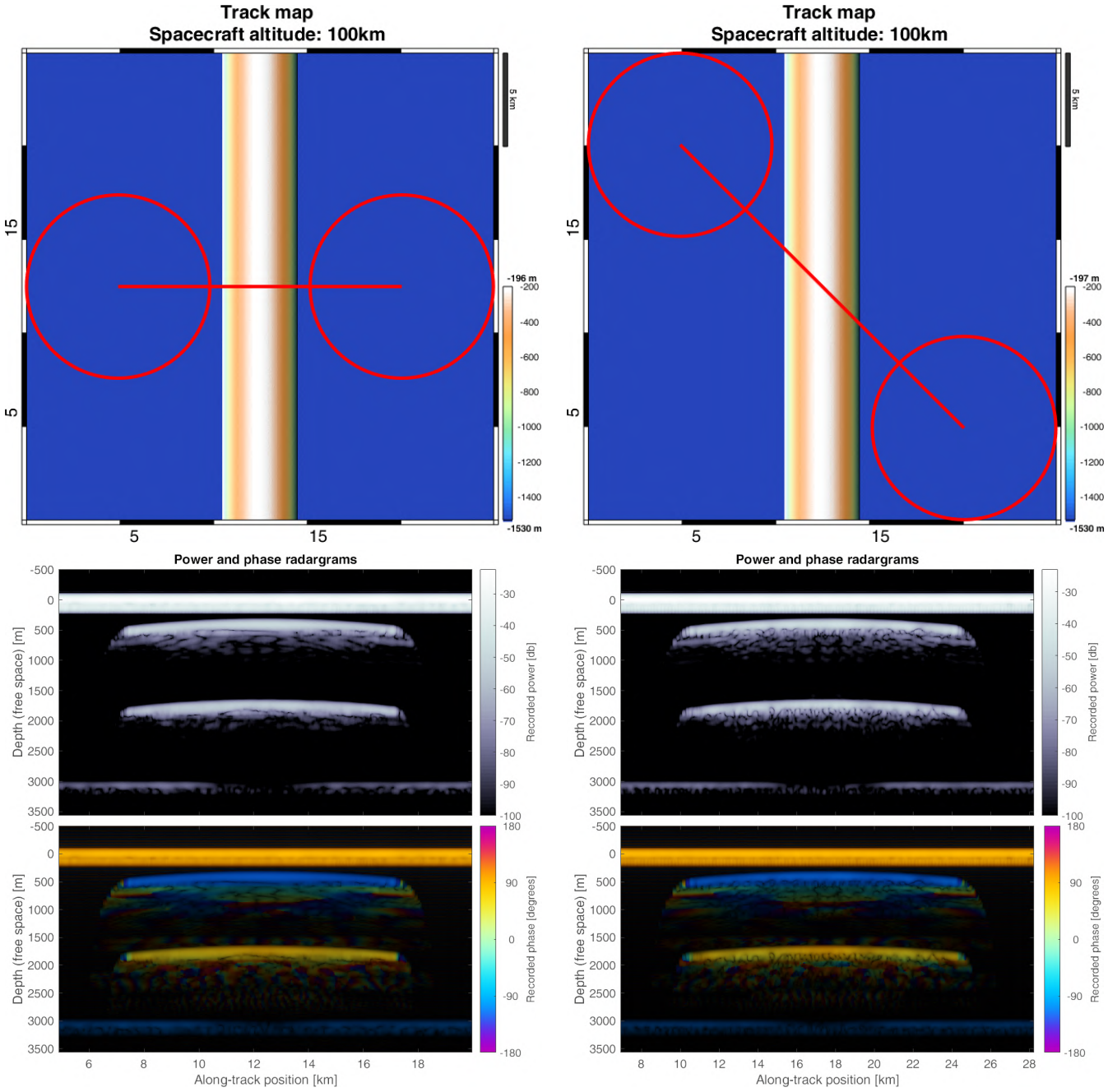

Figure 12: Electromagnetic signature of a lava tube of width w = 4000 m and roof depth h_r = 200m as seen by the 10 MHz central frequency radar. Top : ground tracks of the sounder superimposed on the DEM of the subsurface, containing the lava tube roof, for perpendicular (left) and oblique (right) crossing directions. Bottom : corresponding simulated radargrams. The phase radargrams highlights the phase inversion between the reflection of the roof and the bottom of the lava tube.

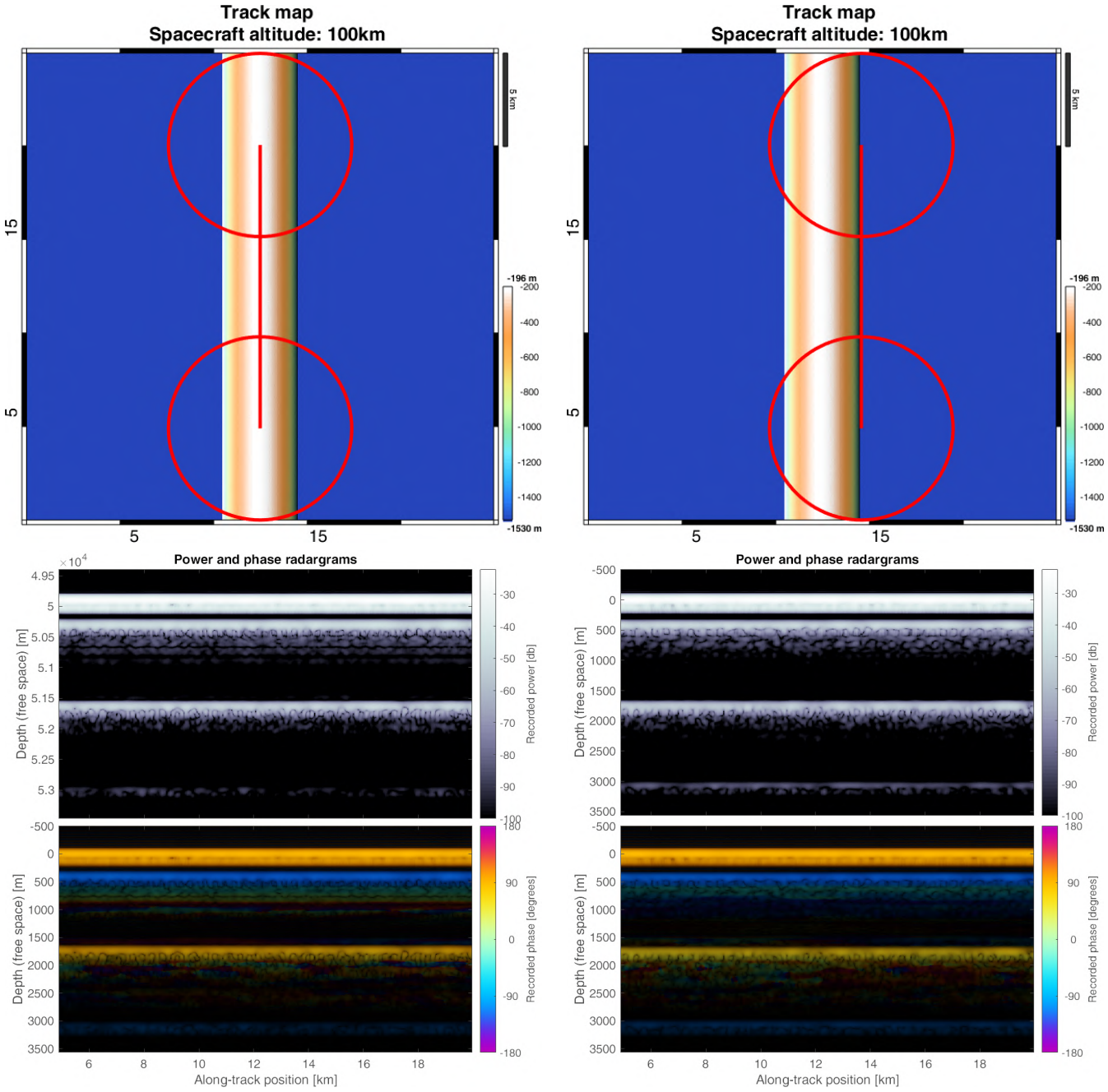

Figure 13: Electromagnetic signature of a lava tube of width w = 4000 m and roof depth h_r = 200m as seen by the 10 MHz central frequency radar. Top : ground tracks of the sounder superimposed on the DEM of the subsurface, containing the lava tube roof, for centred parallel (left) and off-centre parallel (right) crossing directions. Bottom : corresponding simulated radargrams. The phase radargrams highlights the phase inversion between the reflection of the roof and the bottom of the lava tube.

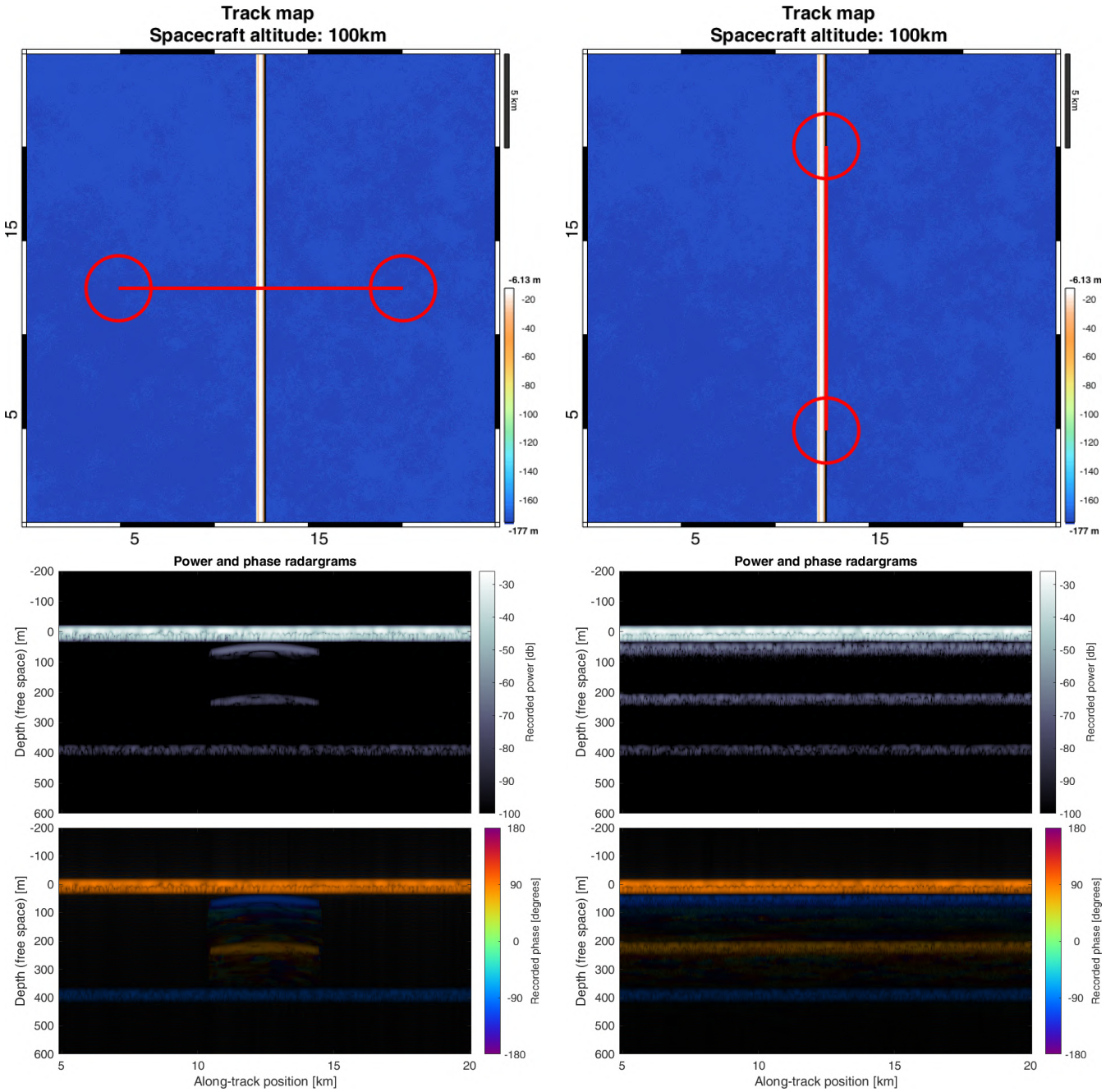

Figure 14: Electromagnetic signature of a lava tube of width w = 500 m and roof depth h_r = 20m as seen by the 60 MHz central frequency radar. Top : ground tracks of the sounder superimposed on the DEM of the subsurface, containing the lava tube roof, for perpendicular (left) and off-centre parallel (right) crossing directions. Bottom : corresponding simulated radargrams. The phase radargrams highlights the phase inversion between the reflection of the roof and the bottom of the lava tube.

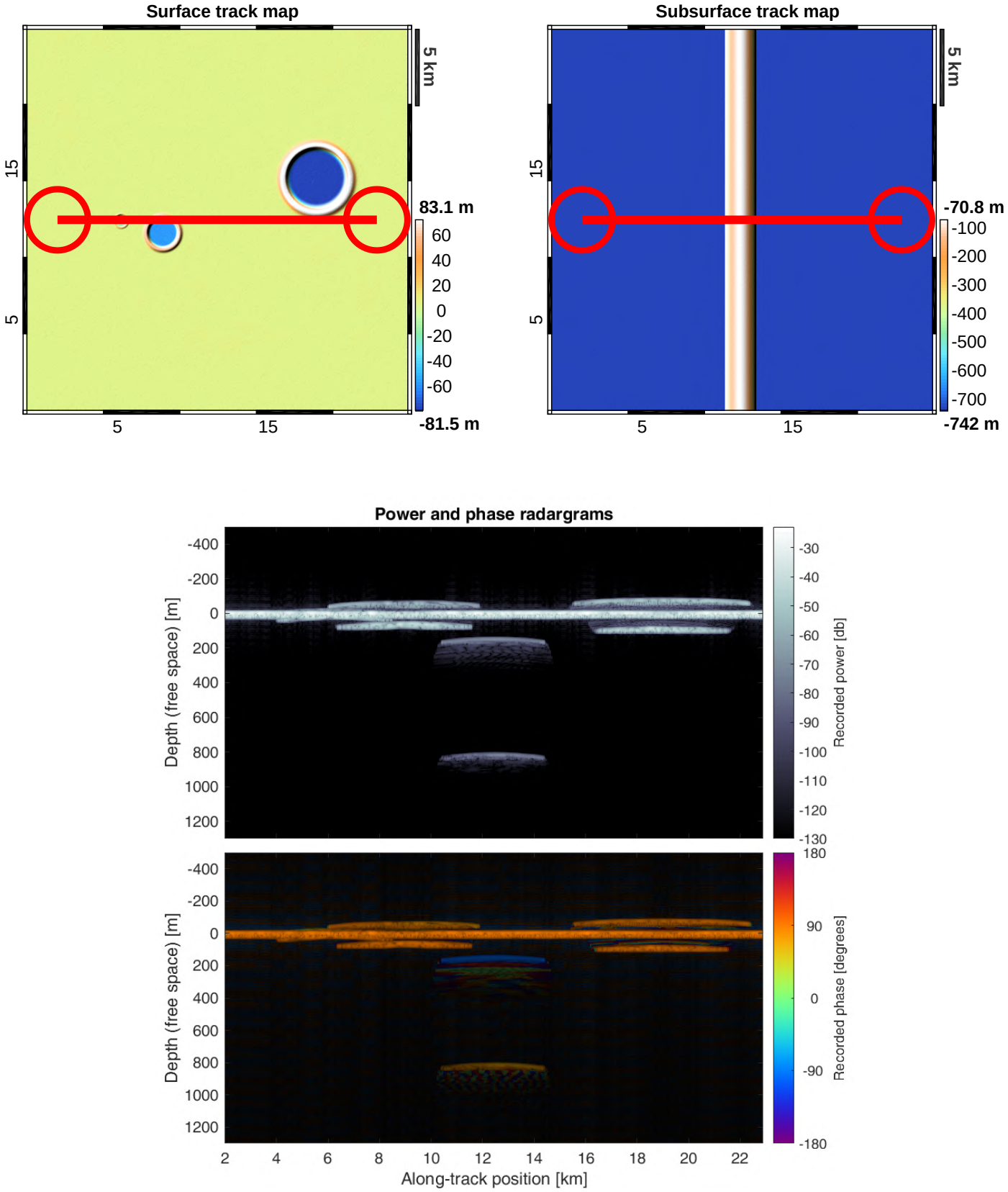

Figure 15: Electromagnetic signature of a w = 2000m tube at a depth h_r = 75 m under a cratered surface as seen by the 60 MHz instrument. Top: Shaded-relief top view of the surface (left) and subsurface (right) DEMs, in which the lava tube roof can be seen, along with the ground track of the probe (red line) and two examples of footprints, the initial one and the final one (red circles). Bottom: Simulated radargram.

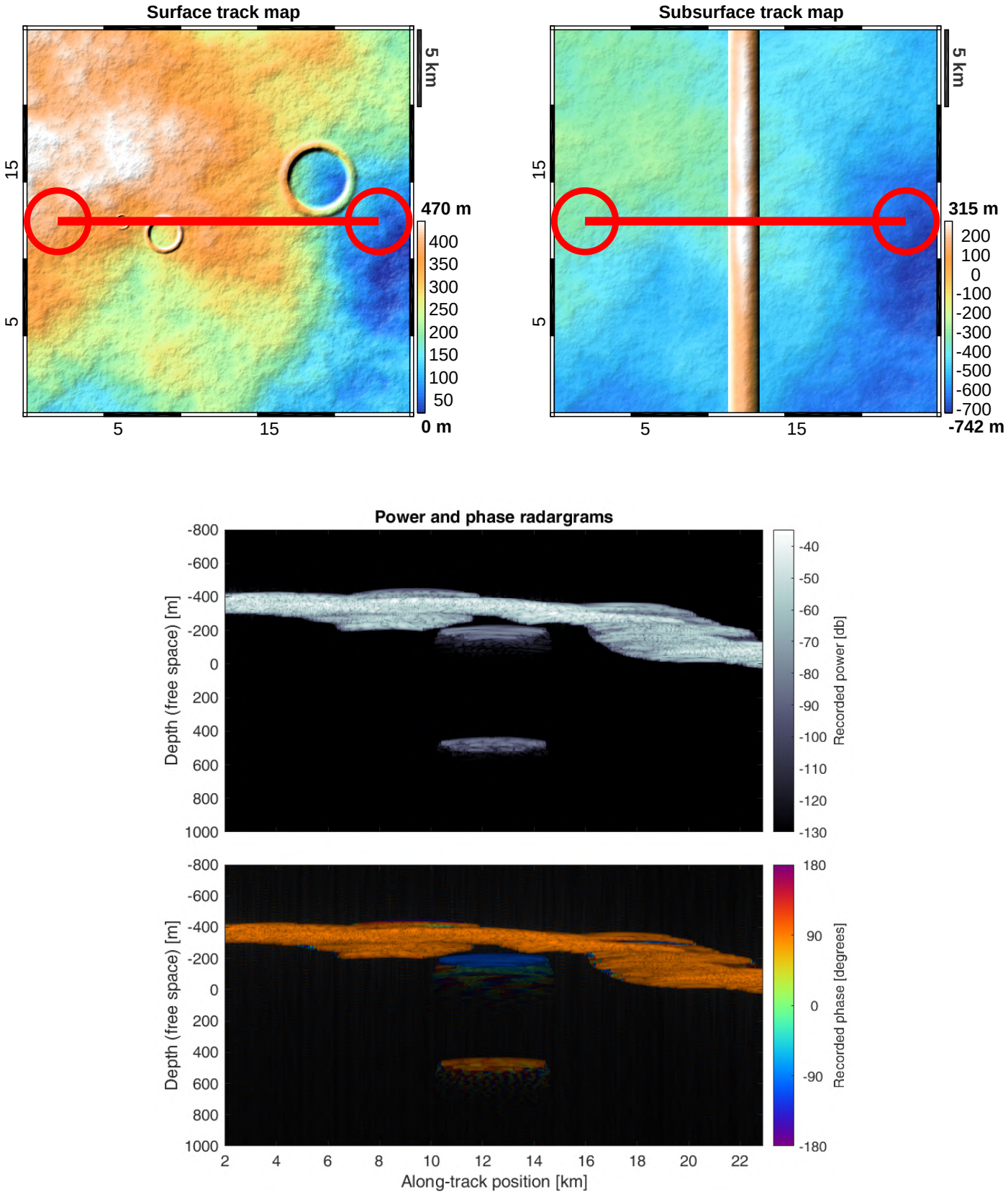

Figure 16: Electromagnetic signature of a w = 2000m tube at a depth h_r = 75 m under a rough cratered surface as seen by the 60 MHz instrument. Top: Shaded-relief top view of the surface (left) and subsurface (right) DEMs, in which the lava tube roof can be seen, along with the ground track of the probe (red line) and two examples of footprints, the initial one and the final one (red circles). Bottom: Simulated radargram.

4.2. *Lava Tubes Electromagnetic Signatures : Impact of Lunar Topography*

The simulations presented in the previous section were performed assuming a flat lunar surface. This allowed to characterize the radar electromagnetic signature of lava tubes in an ideal scenario. In this section, we analyse the effect of lunar topography on the lava tubes electromagnetic signatures. We consider three test scenarios namely (i) a reference case with no roughness, (ii) a case with a cratered surface and (iii) a case with a rough cratered surface and rough subsurface.

We performed the simulations of the above test scenarios considering a lava tube with width equal to $w = 2000\,\text{m}$, and depth of lava tube roof equal to $h_r = 75\,\text{m}$. The radar central frequency has been set equal to $f_0 = 60\,\text{MHz}$ and the associated bandwidth equal to $B = 30\,\text{MHz}$. Compared to the previous experiments, we selected a different central frequency in order to provide additional data.

In the lunar mare region, craters are the surface features which are mainly responsible for subsurface clutter. They are very likely to produce signatures composed of two vertically-aligned hyperbolas, which can be mistaken as lava tubes. The cratered surface simulation was run using a digital elevation model (DEM) including three craters of different sizes (see Fig. 15-top). On the one hand, the discrimination of crater signatures from the lava tube ones based on the power signature is very difficult due to the wide range of shapes craters and lava tubes can take. On the other hand, the signal phase information offers a very strong differentiating criterion. Experimental results show that, whereas hyperbolas of the crater signature display the same phase, those from a lava tube show a clear phase inversion on its upper hyperbola (see Fig. 15-bottom) allowing to discriminate between clutter and lava tubes echoes.

For the rough cratered surface and rough subsurface case, a fBm terrain with $H = 0.78$, $T = 20.6\,\text{m}$, resulting in a RMS slope of $s(\Delta x) = 2.5^\circ$ at $\Delta x = 17\,\text{m}$, was superimposed to the DEM of the previous simulation. The fractal modelling of the surface is a reasonable representation of the lunar mare terrains [22], in which lava tubes have the highest probability of being found. A similar roughness has been applied to the lava tube roof and floor. Setting and results are shown in Fig. 16.

In this simulation, we observe that the roof has an average peak power of -80 dB while the floor as an average power of -85 dB. These values are largely consistent with the findings of the performance analysis. The reference case yielded a peak power of about -70 dB for both the floor and the roof of the lava tube. The subsurface roughness as the effect of slightly distorting the lava tube signature with respect to the reference case. Nevertheless, the lava tube radar response can still be interpreted as two vertically-aligned traces. More importantly, in this noiseless simulation, the surface roughness does not affect the phase information of the lava tube signals preserving the phase inversion mechanism. The response of the craters, although buried in the surface response, also indicates a negligible perturbation of the phase response.

The main conclusion from this analysis is that, even for surface presenting both roughness and clutter sources consistent with those typical of the lunar surface, the findings from the previous section still hold. The mechanism of phase inversion proved to be rather robust with respect to surface topography allowing to discriminate lava tubes from off-nadir surface clutter.

In the case of clutter sources which are not located in the cross-track direction of the spacecraft, frequency analysis could also be used to discriminate between a nadir subsurface return (zero Doppler shift) and a an off-nadir clutter return (non-zero Doppler shift). Moreover clutter can be removed by performing clutter simulations as in [44] by taking advantage of the availability of the digital elevation model. Phase inversion, Doppler analysis and clutter simulations could thus be used in conjunction to further improve the reliability of lava tube detection.

5. Discussion and Conclusions

Recent evidence based on gravity measurements and optical camera surveys suggest that there is a large number of lava tubes concealed under the Moon surface. In this paper we investigated the feasibility of sounding lunar lava tubes of different dimensions from space with an instrument specifically dedicated for this task. By combining a theoretical performance analysis and comprehensive 3D electromagnetic simulations, we assessed the detectability of a wide range of lunar lava tubes.

The results show that a multi-frequency sounder in the MHz range is the best option to satisfactorily detect most of the lava tubes dimension which are expected from structural stability analysis recently presented in the literature with some limitations for small lava tubes. The main driving factors affecting the radar sounding performance are the attenuation of the basalt substrate (i.e. the value of the loss tangent) and its roughness (i.e. base of the regolith relief). The relief of the regolith/substrate interface is estimated to be in the order of meters. Our analysis shows that radar sounding at central frequencies between 80 MHz and 100 MHz can be considerably affected by it depending on the actual heights variation of the relief. By taking into account the sounding limitation imposed by the rough substrate and the 50 % fractional bandwidth assumption, a possible choice of the ranges of the two central frequencies that allow to sound the majority of lava tube dimensions in the Maria region is between 10 and 15 MHz for large lava tubes and between 60 and 65 MHz for small lava tubes.

Regarding the technological readiness level of the proposed system, the fractional bandwidth of 50% can represent a surmountable challenge for the matching network design especially for frequencies in the lower range. The assumption on radiated power is based on the Lunar Radar Sounder transmitted power. The duty cycle in the LRS case is about 0.4%. The very low duty cycle was dictated by the 25% efficiency of the amplifiers. Please note that this configuration does not reflect the current state of the art in HF amplifiers. LRS has been developed more than 10 years ago. Modern amplifiers can reach 50% efficiency. In our case, the duty cycle is 5%, which is a reasonable and technological feasible value nowadays.

We simulated ideal radar signatures by analysing four lava tubes

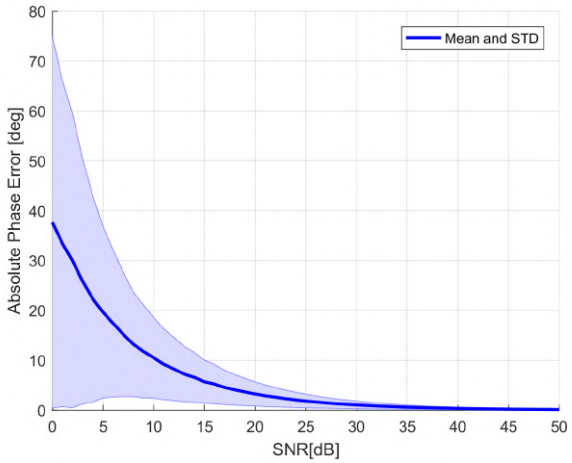

Figure 17: Mean and standard deviation of absolute phase error induced on the echo signal by galactic noise versus SNR.

with representative dimensions. The simulations were performed at two different radar central frequency namely 10 MHz and 60 MHz.

Experimental results show that lava tube signatures (*i.e.*, radar echoes) are composed of two vertically-aligned ensembles hyperbolas, one for the lava tube roof and one for its floor, each made of one bright hyperbola overhanging some more chaotic, dimmer returns. The radar echo from the lava tube roof shows a phase shift of 180° with respect to both the surface and the lava tube floor returns. This constitutes a very strong criterion to differentiate lava tube echoes from clutter (which do not show such phase inversion). The lava tube echoes structure and phase inversion mechanism hold even in the presence of surface roughness such as that characterizing the lunar mare region of the moon. This is an important result as lunar mares are the main candidate regions for the subsurface presence of lava tubes.

This study suffer from a certain number of limitations. The theoretical calculation of the range resolution estimation neglects the surface response that elongates over many different range bins depending on the surface characteristics an the actual radar antenna pattern. This could cause an overestimation of the detectability of the shallowest tubes. This effect has been detected in the simulations where lava tubes with sizes on the edge of detectability in the performance analysis could not be distinguished from the surface echo. The simulator itself has a limitation as well regarding whether or not the actual lunar surface topography is considered. As a coherent-only algorithm, it is forced to neglect any electromagnetic interaction at scales smaller to that of the DEM used, which in this case has a resolution of 118 m. This may have limited the amount of diffuse scattering in the simulated radargrams.

The future direction of our work is to analyse Moon radar sounding data recorded by the LRS instrument and verify whether there are evidence of the lava tubes electromagnetic signatures presented in this paper. This can be done by taking into account the inherent limitation of LRS in terms of lava tubes detection capability being the system not specifically designed for this task.

References

[1] I. A. Crawford, Lunar resources: A review, Progress in Physical Geography 39 (2) (2015) 137–167.

[2] F. Horz, Lava tubes - Potential shelters for habitats, in: W. W. Mendell (Ed.), Lunar Bases and Space Activities of the 21st Century, 1985, pp. 405–412.

[3] R. Greeley, Introduction to Planetary Geomorphology, Cambridge University Press, 2013.
URL https://books.google.it/books?id=fZwNNP-IzicC

[4] G. De Angelis, J. Wilson, M. Clowdsley, J. Nealy, D. Humes, J. Clem, Lunar lava tube radiation safety analysis, Journal of radiation research 43 (S) (2002) S41–S45.

[5] D. M. Blair, L. Chappaz, R. Sood, C. Milbury, A. Bobet, H. J. Melosh, K. C. Howell, A. M. Freed, The structural stability of lunar lava tubes, Icarus 282 (2017) 47 – 55. doi:http://dx.doi.org/10.1016/j.icarus.2016.10.008.
URL http://www.sciencedirect.com/science/article/pii/S0019103516

[6] L. Chappaz, R. Sood, H. J. Melosh, K. C. Howell, D. M. Blair, C. Milbury, M. T. Zuber, Evidence of large empty lava tubes on the moon using grail gravity, Geophysical Research Letters 44 (1) (2017) 105–112.

[7] A. Arya, R. Rajasekhar, G. Thangjam, A. Kumara, A. Kiran Kumara, Detection of potential site for future human habitability on the moon using chandrayaan-1 data., Current Science (00113891) 100 (4).

[8] J. Haruyama, K. Hioki, M. Shirao, T. Morota, H. Hiesinger, C. H. van der Bogert, H. Miyamoto, A. Iwasaki, Y. Yokota, M. Ohtake, et al., Possible lunar lava tube skylight observed by selene cameras, Geophysical Research Letters 36 (21).

[9] B. A. Campbell, B. Ray Hawke, G. A. Morgan, L. M. Carter, D. B. Campbell, M. Nolan, Improved discrimination of volcanic complexes, tectonic features, and regolith properties in mare serenitatis from earth-based radar mapping, Journal of Geophysical Research: Planets 119 (2) (2014) 313–330.

[10] L. J. Porcello, R. L. Jordan, J. S. Zelenka, G. F. Adams, R. J. Phillips, W. E. Brown, S. H. Ward, P. L. Jackson, The apollo lunar sounder radar system, Proceedings of the IEEE 62 (6) (1974) 769–783. doi:10.1109/PROC.1974.9517.

[11] T. Ono, H. Oya, Lunar radar sounder (lrs) experiment on-board the selene spacecraft, Earth, Planets and Space 52 (9) (2000) 629–637. doi:10.1186/BF03351671.
URL http://dx.doi.org/10.1186/BF03351671

[12] J. Haruyama, T. Kaku, R. Shinoda, W. Miyake, A. Kumamoto, K. Ishiyama, T. Nishibori, K. Yamamoto, K. Kurosawa, A. Suzuki, et al., Detection of lunar lava tubes by lunar radar sounder onboard selene (kaguya), in: Lunar and Planetary Science Conference, Vol. 48, 2017.

[13] T. Kaku, J. Haruyama, W. Miyake, A. Kumamoto, K. Ishiyama, T. Nishibori, K. Yamamoto, S. T. Crites, T. Michikami, Y. Yokota, et al., Detection of intact lava tubes at marius hills on the moon by selene (kaguya) lunar radar sounder, Geophysical Research Letters.

[14] R. Sood, H. J. Melosh, K. Howell, Lunar advanced radar orbiter for subsurface sounding (laross): lava tube exploration mission, in: AAS/AIAA 26th Space Flight Mechanics Meeting, 2016.

[15] H. Miyamoto, J. Haruyama, T. Kobayashi, K. Suzuki, T. Okada, T. Nishibori, A. P. Showman, R. Lorenz, K. Mogi, D. A. Crown, et al., Mapping the structure and depth of lava tubes using ground penetrating radar, Geophysical research letters 32 (21).

[16] C. R. Rowell, A. Pidlisecky, J. D. Irving, R. J. Ferguson, Characterization of lava tubes using ground penetrating radar at craters of the moon national monument, usa., Tech. rep., CREWES Research Report, 22, 1-18 (2010).

[17] G. R. Olhoeft, D. Sinex, K. Sander, M. Lagmanson, D. Stillman, S. Lewis, B. Clark, E. Wallin, J. Kauahikaua, Hot and cold lava tube characterization with ground penetrating radar, in: 8th International Conference on Ground Penetrating Radar, International Society for Optics and Photonics, 2000, pp. 482–487.

[18] C. R. Coombs, B. Hawke, A search for intact lava tubes on the moon: Possible lunar base habitats, in: Lunar Bases and Space Activities of the 21st Century, 1992.

[19] K. A. Howard, J. W. Head, G. A. Swann, Geology of hadley rille.

[20] M. Robinson, J. Ashley, A. Boyd, R. Wagner, E. Speyerer, B. R. Hawke, H. Hiesinger, C. Van Der Bogert, Confirmation of sublunarean voids and thin layering in mare deposits, Planetary and Space Science 69 (1) (2012) 18–27.

[21] W. Fa, M. A. Wieczorek, E. Heggy, Modeling polarimetric radar scattering from the lunar surface: Study on the effect of physical properties of the regolith layer, Journal of Geophysical Research: Planets 116 (E3).

[22] M. Rosenburg, O. Aharonson, J. Head, M. Kreslavsky, E. Mazarico, G. A. Neumann, D. E. Smith, M. H. Torrence, M. T. Zuber, Global surface slopes and roughness of the moon from the lunar orbiter laser altimeter, Journal of Geophysical Research: Planets 116 (E2).

[23] Y. G. Shkuratov, N. V. Bondarenko, Regolith layer thickness mapping of the moon by radar and optical data, Icarus 149 (2) (2001) 329–338.

[24] B. Campbell, Radar Remote Sensing of Planetary Surfaces, Cambridge University Press, 2002.
URL https://books.google.it/books?id=qlxB-_X0-G0C

[25] G. R. Olhoeft, D. Strangway, Dielectric properties of the first 100 meters of the moon, Earth and Planetary Science Letters 24 (3) (1975) 394–404.

[26] F. T. Ulaby, D. G. Long, W. J. Blackwell, C. Elachi, A. K. Fung, C. Ruf, K. Sarabandi, H. A. Zebker, J. Van Zyl, Microwave radar and radiometric remote sensing, Vol. 4, University of Michigan Press Ann Arbor, 2014.

[27] G. Picardi, D. Biccari, R. Seu, L. Marinangeli, W. Johnson, R. Jordan, J. Plaut, A. Safaenili, D. Gurnett, G. Ori, et al., Performance and surface scattering models for the mars advanced radar for subsurface and ionosphere sounding (marsis), Planetary and Space Science 52 (1) (2004) 149–156.

[28] S. M. Clifford, A model for the hydrologic and climatic behavior of water on mars, Journal of Geophysical Research: Planets 98 (E6) (1993) 10973–11016.

[29] D. Biccari, D. Calabrese, D. Gurnett, R. Huff, L. Marinangeli, R. Jordan, E. Nielsen, G. Ori, G. Picardi, J. PIaut, et al., Venus subsurface ionosphere radar sounder: Vensis, in: 3D Data Processing, Visualization and Transmission, 2004. 3DPVT 2004. Proceedings. 2nd International Symposium on, IEEE, 2004, pp. 931–937.

[30] D. W. Strangway, G. R. Olhoeft, Electrical properties of planetary surfaces, Philosophical Transactions of the Royal Society of London A: Mathematical, Physical and Engineering Sciences 285 (1327) (1977) 441–450. arXiv:http://rsta.royalsocietypublishing.org/content/285/1327/441.full.pdf, doi:10.1098/rsta.1977.0086.
URL http://rsta.royalsocietypublishing.org/content/285/1327/441

[31] W. D. Carrier, G. R. Olhoeft, W. Mendell, Physical properties of the lunar surface, Lunar sourcebook (1991) 475–594.

[32] L. Bruzzone, G. Alberti, C. Catallo, A. Ferro, W. Kofman, R. Orosei, Subsurface radar sounding of the jovian moon ganymede, Proceedings of the IEEE 99 (5) (2011) 837–857.

[33] D. M. Schroeder, C. Grima, D. D. Blankenship, Evidence for variable grounding-zone and shear-margin basal conditions across thwaites glacier, west antarctica, Geophysics 81 (1) (2015) WA35–WA43.

[34] M. E. Peters, D. D. Blankenship, D. L. Morse, Analysis techniques for coherent airborne radar sounding: Application to west antarctic ice streams, Journal of Geophysical Research: Solid Earth 110 (B6).

[35] L. Boithias, L.-J. Libols, Radio wave propagation, North Oxford acad. London, 1987.

[36] T. Hagfors, Backscattering from an undulating surface with applications to radar returns from the moon, Journal of Geophysical Research 69 (18) (1964) 3779–3784. doi:10.1029/JZ069i018p03779.
URL http://dx.doi.org/10.1029/JZ069i018p03779

[37] J. D. Kraus, Radio astronomy, 2-nd ed, Cygnus-Quasar Books, Powell, Ohio (1986) 7–12.

[38] D. M. Schroeder, A. Romero-Wolf, L. Carrer, C. Grima, B. A. Campbell, W. Kofman, L. Bruzzone, D. D. Blankenship, Assessing the potential for passive radio sounding of europa and ganymede with rime and reason, Planetary and Space Science 134 (2016) 52 – 60. doi:http://dx.doi.org/10.1016/j.pss.2016.10.007.
URL http://www.sciencedirect.com/science/article/pii/S0032063316

[39] B. A. Campbell, Scale-dependent surface roughness behavior and its impact on empirical models for radar backscatter, IEEE Transactions on Geoscience and Remote Sensing 47 (10) (2009) 3480–3488. doi:10.1109/TGRS.2009.2022752.

[40] V. Mikhnev, P. Vainikainen, Characterization of underground objects in uwb gpr by range profiling of phase, in: Radar Conference (EuRAD), 2010 European, IEEE, 2010, pp. 368–371.

[41] V. Mikhnev, M.-K. Olkkonen, E. Huuskonen, Subsurface target identification using phase profiling of impulse gpr data, in: Ground Penetrating Radar (GPR), 2012 14th International Conference on, IEEE, 2012, pp. 376–380.

[42] B. Sai, L. P. Ligthart, Gpr phase-based techniques for profiling rough surfaces and detecting small, low-contrast landmines under flat ground, IEEE Transactions on Geoscience and Remote Sensing 42 (2) (2004) 318–326.

[43] E. Huuskonen-Snicker, V. A. Mikhnev, M.-K. Olkkonen, Discrimination of buried objects in impulse gpr using phase retrieval technique, IEEE Transactions on Geoscience and Remote Sensing 53 (2) (2015) 1001–1007.

[44] A. Ferro, A. Pascal, L. Bruzzone, A novel technique for the automatic detection of surface clutter returns in radar sounder data, IEEE Transactions on Geoscience and Remote Sensing 51 (5) (2013) 3037–3055.